

RESEARCH ARTICLE

10.1002/2015JD023645

Key Points:

- WRF reproduces the observed convection well
- The upper level outflow is from two different convective systems
- Lightning contributes substantially to NO in the outflow

Correspondence to:

L. W. Siu,
slwchris@neo.tamu.edu

Citation:

Siu, L. W., K. P. Bowman, and C. C. Epifanio (2015), Convective transport of trace species observed during the Stratosphere-Troposphere Analyses of Regional Transport 2008 experiment, *J. Geophys. Res. Atmos.*, *120*, 10,530–10,547, doi:10.1002/2015JD023645.

Received 7 MAY 2015

Accepted 7 SEP 2015

Accepted article online 12 SEP 2015

Published online 5 OCT 2015

Convective transport of trace species observed during the Stratosphere-Troposphere Analyses of Regional Transport 2008 experiment

Leong Wai Siu¹, Kenneth P. Bowman¹, and Craig C. Epifanio¹¹Department of Atmospheric Sciences, Texas A&M University, College Station, Texas, USA

Abstract During the Stratosphere-Troposphere Analyses of Regional Transport 2008 experiment (START08) the NCAR/NSF Gulfstream V aircraft observed high concentrations of NO and NO_y in the upper troposphere downwind of a weakening squall line in northern Texas, suggesting either convective transport of polluted boundary layer air to the upper troposphere or lightning production of nitrogen oxides in the convection. These hypotheses are tested by computing three-dimensional back trajectories using winds from a high-resolution simulation of the event with the Weather Research and Forecasting (WRF) model. The WRF model simulation reproduces the storm structure and evolution with good fidelity. The back trajectories reveal two distinct layers of outflow air from different mesoscale convective systems (MCSs). Most air in the upper layer is transported northward from an MCS in southern Texas, while the lower layer is from both the northern squall line and the southern MCS. In both layers inconsistencies between observed concentrations of CO, NO, and O₃ and predictions from a simple mixing model suggest that there is significant production of NO by lightning in the convective systems. This is consistent with lightning observations from the National Lightning Detection Network. Additionally, the model simulation appears to slightly underestimate the depth of vertical transport by the MCS.

1. Introduction

Each year around 100,000 thunderstorms take place in the U.S. [Jaeglé, 2007]. Convective transport by thunderstorms has long been known to have an important influence on the chemical composition of the upper troposphere (UT) [e.g., Dickerson *et al.*, 1987; Pickering *et al.*, 1990; Poulida *et al.*, 1996; Ridley *et al.*, 2004a; Bertram *et al.*, 2007]. In a convective system, the characteristic vertical velocity of updraft cores can be more than 16 m s⁻¹ [Dye *et al.*, 2000], which gives a vertical transport time through the depth of the troposphere of less than an hour [Bertram *et al.*, 2007]. Compared with the boundary layer (BL), reaction rates, except photolysis, are usually reduced in the rather cold and dry UT. The result is that, once lofted to the UT, and in some cases into the lower stratosphere (LS), many trace gases have chemical lifetimes that are longer than the convective transport time. Also, while the typical size of a convective system is on the order of 100 km, trace gases in the UT can be carried by upper level winds around the globe and can stay in the UT for more than a week [Stenchikov *et al.*, 1996; Ridley *et al.*, 2004a]. Deep convection impacts the global climate in two principal ways. First, ozone (O₃) and aerosols are produced by chemical reactions of trace gases in the UT. Second, water vapor (H₂O) is transported from the moist lower troposphere (LT) to the UT, where it is the major greenhouse gas [Lacis *et al.*, 1990; Jaeglé, 2007].

Tropospheric chemistry plays an important role in both the production and destruction of tropospheric ozone [Liu *et al.*, 1980]. Ozone precursors, particularly NO_x (NO + NO₂), hydrocarbons, and carbon monoxide (CO), are responsible for producing O₃ through a series of photochemical reactions [Bradshaw *et al.*, 2000]. For example, NO_x acts as a catalyst in producing O₃ during the oxidation of CO to carbon dioxide (CO₂). The lifetime of NO_x extends from about 1 to 2 days in the BL to 2 weeks in the UT, but it is still much shorter than CO, which has a lifetime of a few months [Ehhalt and Rohrer, 1995; Seinfeld and Pandis, 2006]. The amount of NO_x is low in the troposphere because it is very reactive [Logan, 1983]. This makes NO_x a rate-determining tracer in the above processes [Lelieveld and Crutzen, 1994; Crutzen and Lelieveld, 2001]. During daytime, NO is favored under the NO_x partition in the UT while NO₂ is favored under the same partition in the BL [Seinfeld and Pandis, 2006]. Using a one-dimensional photochemical model, Pickering *et al.* [1990] show that ozone precursors at the Earth's surface can enhance the production of upper tropospheric ozone fourfold.

It is important to determine the distribution of NO_x in the troposphere and its production and removal mechanisms. The major sources of NO_x in the BL include fossil fuel combustion, biomass burning, and emissions from the soil or oceans, whereas stratospheric intrusions, lightning, and aircraft emissions contribute the most to NO_x in the free troposphere [Bradshaw *et al.*, 2000; Crutzen and Lelieveld, 2001]. The production of NO from lightning is particularly important because it is associated with deep convection in thunderstorms. Using a global three-dimensional chemical transport model, Zhang *et al.* [2003] show that summer lightning has a chief role in controlling both the concentrations of NO_x and O_3 in the MT and UT. The distribution of tropospheric NO_x , however, remains highly uncertain. For example, NO_x emission from lightning has been estimated to be between 2 and 20 Tg N yr^{-1} , which means it could be either a small source or a major contributor to tropospheric NO_x [DeCaria *et al.*, 2000]. Recent estimation has constrained the value to be between 2 and 8 Tg N yr^{-1} [Schumann and Huntrieser, 2007].

Many observational and modeling studies have been devoted to examining the influence of convective transport by midlatitude thunderstorms, especially in the anvil region [e.g., Dickerson *et al.*, 1987; Skamarock *et al.*, 2000; Ridley *et al.*, 2004b]. Large-scale models typically parameterize convective transport. With sufficient resolution, mesoscale models can explicitly simulate convection, but they still rely on parameterizations of microphysical processes, subgrid-scale transport processes, and atmospheric radiation. Barth *et al.* [2007] show that high-resolution mesoscale models are able to reproduce observed storm structure and kinematics in specific simulations, and air parcel trajectories can help to understand transport pathways and determine the origin of selected air masses. For example, Jaeglé *et al.* [1997] compute the concentrations of hydrogen peroxide (H_2O_2), methyl hydroperoxide (CH_3OOH), and formaldehyde (CH_2O) along isentropic trajectories and use the result to justify the underestimation of hydroperoxyl (HO_2) in the model. Skamarock *et al.* [2000] demonstrate from trajectory analysis that the anvil air in a simulated multicellular convective system rose up from a layer between 0.5 and 2 km above the surface.

The main objective of this study is to determine the origins and transport pathways of air in the outflow region of a squall line system observed during the Stratosphere-Troposphere Analyses of Regional Transport 2008 (START08) field campaign. Trace gas measurements from the aircraft show two distinct outflow layers ahead of the squall line. It is hypothesized that these outflows are transported from the BL and LT to the UT by the squall line. To test this hypothesis, the squall line system is simulated with a three-dimensional (3-D) nonhydrostatic model. The model produces a good simulation of the squall line in terms of the vertical and horizontal structures of the storm. We use multiple in situ trace gas measurements from START08 and data from the National Lightning Detection Network (NLDN) to deduce the sources of NO and total reactive nitrogen ($\text{NO}_y = \text{NO}_x +$ all compounds from the oxidation of NO_x) observed in the outflow air.

2. Data and Methods

2.1. Aircraft Observations

From April to June of 2008, the START08 field campaign used the National Science Foundation/National Center for Atmospheric Research (NSF/NCAR) Gulfstream V (GV) aircraft to study the chemical and dynamical characteristics of the midlatitude upper troposphere and lower stratosphere [Pan *et al.*, 2010]. Eighteen research flights (RF01–RF18) with a total of 123 flight hours extensively covered central North America and the Gulf of Mexico between $\sim 25^\circ$ – 65°N and $\sim 120^\circ$ – 85°W . The standard instruments on the aircraft measured state parameters such as position, altitude, ambient air temperature, and humidity. The aircraft was also equipped with instruments to measure atmospheric trace gases and microphysical parameters. Trace gas observations from Research Flight 8 (RF08), including O_3 , CO, NO, and NO_y are analyzed in this study (Table 1). Some periods of negative NO and NO_y values are found in the free troposphere, where both NO and NO_y concentrations are generally low. This indicates a likely bias error in the measurements, so all NO and NO_y measurements are offset by adding 57.3 pptv and 20.0 pptv, respectively (A. Weinheimer, personal communication, 2015).

2.2. Radar Data

Radar data, which are archived at the National Climatic Data Center, come from the Next Generation Weather Radar (NEXRAD) system. This program collects data from the Weather Surveillance Radar-1988 Doppler (WSR-88D) network [Crum *et al.*, 1993]. This study uses Level II reflectivity data from individual radars. The data span the period from 5 to 7 May and cover the middle U.S. (Figure 1). There was a transitional period between May and August 2008 in which the NEXRAD network was upgraded for higher-resolution volume scans. During this period some data have an azimuthal resolution of 0.5° and a radial resolution of 0.25 km,

Table 1. GV Research Instruments Used in This Study^a

Instruments	Measurements	Properties
Dual-beam UV absorption ozone photometer [Proffitt and McLaughlin, 1983]	O ₃	Lowest detection limit: 1.5×10^{10} molecules cm ⁻³ /0.6 ppbv at STP (one sigma); Maximum uncertainty: 3.6% (at 22 km).
Vacuum-ultraviolet resonance fluorescence (VURF) [Gerbig et al., 1999]	CO	Precision: ± 1.5 ppbv; Uncertainty: 2.4%.
NCAR nitric oxide and total reactive nitrogen [Ridley et al., 2004b]	NO, NO _y	Precision: ~ 5 – 10 pptv; Uncertainty: $\sim 10\%$.

^aAll instruments provide data at 1 Hz.

while other data have an azimuthal resolution of 1° and a radial resolution of 1 km. The higher azimuthal and radial resolution scans lead to a more detailed horizontal storm structure and a greater dynamic range in reflectivity for individual storms. The individual volume scans are combined into three-dimensional gridded radar reflectivity fields using the method described in Homeyer [2014]. In this paper we show two-dimensional vertical sections through the three-dimensional volumes and radar reflectivity maps, which display the maximum radar reflectivity value in each vertical column. The processed composites have a horizontal grid spacing of $0.02^\circ \times 0.02^\circ$, a vertical grid spacing of 1 km, and a time spacing of 5 min.

2.3. Lightning Data

Lightning data are provided by the ground-based U.S. National Lightning Detection Network (NLDN) which tracks lightning activities across the continental U.S. (CONUS) [Orville, 2008]. The network consists of more than 114 lightning sensors. We use data that are reprocessed and archived for nonreal-time users. The data contain date and time, location (in latitude and longitude), peak current (in kA), and strokes per flash (multiplicity) of each lightning event during the field campaign. At the time of the START08 campaign, the system could only detect cloud-to-ground (CG) flashes. The CG flash detection efficiency of the network is estimated to be better than 90% for the continental United States [Orville et al., 2011]. Boccippio et al. [2001] estimate that the ratio of intracloud (IC) to CG lightning over the United States is approximately 3 to 1.

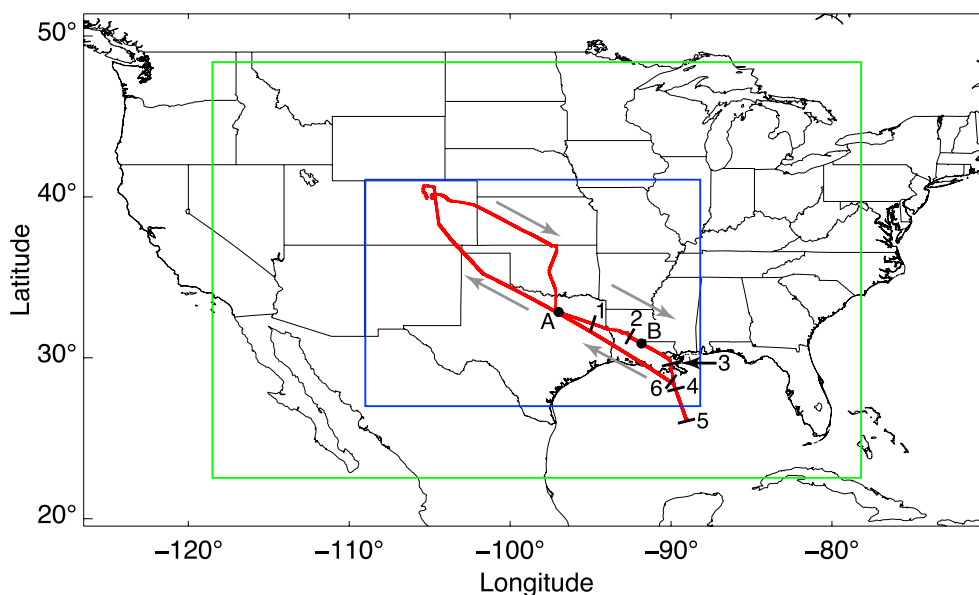


Figure 1. Map of the study area. The blue and green boxes indicate the inner and outer domains of the WRF model, respectively. The red curve is the ground track of the aircraft for START08 Research Flight 8. The flight direction is indicated by the gray arrows. The primary subject of this paper is the portion of the flight between the points labeled A and B (see Figures 2 and 3 for details). The black tick marks indicate the beginning and end of deep profiles shown in Figure 9 that extend from the stratosphere to the boundary layer: 1–2, descent; 2–3, ascent; 4–5, descent; and 5–6, ascent.

The horizontal mass flux of lightning-produced nitrogen oxide (LNO_x) from an anvil is approximated following Chameides *et al.* [1987] and Huntrieser *et al.* [2008] as

$$F_{\text{LNO}_x} = \chi_{\text{LNO}_x} \cdot \frac{M_N}{M_{\text{air}}} \cdot \rho_a \cdot |\vec{V}_a - \vec{V}_s| \cdot \Delta x \cdot \Delta z \quad (1)$$

where F_{LNO_x} is the nitrogen mass flux produced by lightning (g s^{-1}), χ_{LNO_x} is the mean NO_x volume mixing ratio produced by lightning (ppbv), M_N is the molar mass of nitrogen (14 g mol^{-1}), M_{air} is the molar mass of air (29 g mol^{-1}), ρ_a is the air density at the anvil (kg m^{-3}), \vec{V}_a is the horizontal wind velocity in the anvil (m s^{-1}), \vec{V}_s is the wind velocity of the convective system (m s^{-1}), Δx is the width of the anvil (km), and Δz is the depth of the anvil (km). The production rate of LNO_x is calculated using

$$P_{\text{LNO}_x} = \frac{F_{\text{LNO}_x}}{R_{\text{NLDN}} \cdot M_N} \quad (2)$$

where P_{LNO_x} is the number of moles of LNO_x produced in each flash (mol flash^{-1}), F_{LNO_x} is the nitrogen mass flux calculated from equation (1), R_{NLDN} is the NLDN total flash rate (flash s^{-1}), and M_N is the molar mass of nitrogen (14 g mol^{-1}).

3. Models

We use the NCAR Weather Research and Forecasting (WRF) model with the Advanced Research WRF (ARW, version 3.2.1) dynamical solver to simulate the squall line observed during RF08. The model is configured with two domains (Figure 1) with two-way interaction between the domains. A regular latitude-longitude grid is used for the simulations. The horizontal grid spacings of the inner and outer domains are $0.027^\circ \times 0.033^\circ$ and $0.081^\circ \times 0.099^\circ$ (latitude \times longitude), respectively, which are $\sim 3 \text{ km} \times \sim 3 \text{ km}$ and $\sim 9 \text{ km} \times \sim 9 \text{ km}$ when measured near the center of the inner grid. The model has 45 vertical layers at full (mass) levels in η coordinates from the ground to 50 hPa. The vertical spacing increases with altitude, ranging from 200 m in the LT to 510 m in the UT. The WRF time step size of the inner and outer domains are 15 s and 45 s, respectively. To facilitate trajectory [Bowman *et al.*, 2013], model variables are archived every 18 time steps in the inner domain and six time steps in the outer domain (270 s or 4.5 min in both domains). The model is also used to calculate the tropopause height using the World Meteorological Organization algorithm as outlined by Homeyer *et al.* [2010]. Output is linearly interpolated into other vertical coordinates when necessary.

The simulation is initialized with the National Centers for Environmental Prediction (NCEP) Eta 212 grid (40 km) 3-hourly model analysis and run for a period of 42 h from 12:00 UTC 5 May 2008 to 06:00 UTC 7 May 2008. The primary period of interest for this study is 00:00 UTC to 18:00 UTC 6 May, which occurs 12 to 30 h after the beginning of the simulation. Boundary conditions for the outer domain of the model come from the NCEP Eta 212 analysis and NOAA real-time global (RTG) sea surface temperature data. Model variables in the outer domain are nudged to the Eta analysis throughout the simulation, while variables in the inner domain are only nudged for the first 6 h. There is no nudging of temperature and moisture in the BL.

A set of physical parameterization schemes is used to represent the subgrid-scale processes in the model (Table 2). An implicit gravity wave damping layer is applied to the uppermost 6 km in both domains. This damping controls reflection from the upper boundary. We use NCAR Command Language (NCL) utilities to compute the simulated radar reflectivity of the model for comparison with observations.

Because this study is concerned with convective transport, we trace transport pathways for selected air parcels using the TRAJ3D trajectory model [Bowman, 1993; Bowman and Carrie, 2002]. Backward trajectories are computed off-line for 24 h using the simulated WRF wind fields saved every 270 s (321 time steps in total). This integration period covers the relevant part of the life cycle of the observed squall line and captures the vertical convective transport of the target air parcels during that period.

Given the source regions of the parcels from the back trajectories and the concentrations of trace gases from a profile measured by the GV as it descended from the lower stratosphere to the boundary layer ahead of the squall line, we estimate the concentration of CO , NO , and O_3 in the outflow layers according to

$$C = f_{\text{LS}} \cdot C_{\text{LS}} + f_{\text{UT}} \cdot C_{\text{UT}} + f_{\text{MT}} \cdot C_{\text{MT}} + f_{\text{LT}} \cdot C_{\text{LT}} + f_{\text{BL}} \cdot C_{\text{BL}} \quad (3)$$

Table 2. Physical Parameterizations of the WRF Model Run^a

Type of Parameterization	Schemes
Microphysics	Goddard five-species, single-moment microphysics scheme [Tao et al., 1989]
Cumulus	Betts-Miller-Janjic (BMJ) scheme [Janjić, 1994]
Planetary boundary layer	Yonsei University (YSU) scheme [Hong et al., 2006]
Land surface	Noah land-surface model [Tewari et al., 2004]
Surface layer	MM5 Similarity scheme [Beljaars, 1995]
Longwave radiation	Rapid Radiative Transfer Model (RRTM) [Mlawer et al., 1997]
Shortwave radiation	Goddard shortwave scheme [Chou and Suarez, 1994]

^aThe cumulus parameterization is only applied to the outer domain.

where f is the fraction of parcels from each source region and C is the concentration of a given species within those source regions. Source regions are designated as lower stratosphere (LS), upper troposphere (UT), middle troposphere (MT), lower troposphere (LT), and boundary layer (BL).

As will be seen in the trajectory model results, the sources of air for the convective updrafts come from a large geographic region. It was not possible to make in situ observations of trace species concentrations over this large area, so we assume that the trace species concentrations in the layers are horizontally homogeneous and estimate these concentrations from the aircraft descent profile made ahead of the squall line. Additional deep profiles observed during the flight indicate that this is a reasonable assumption. The values selected for the concentrations in the source regions are discussed in section 4.3.1.

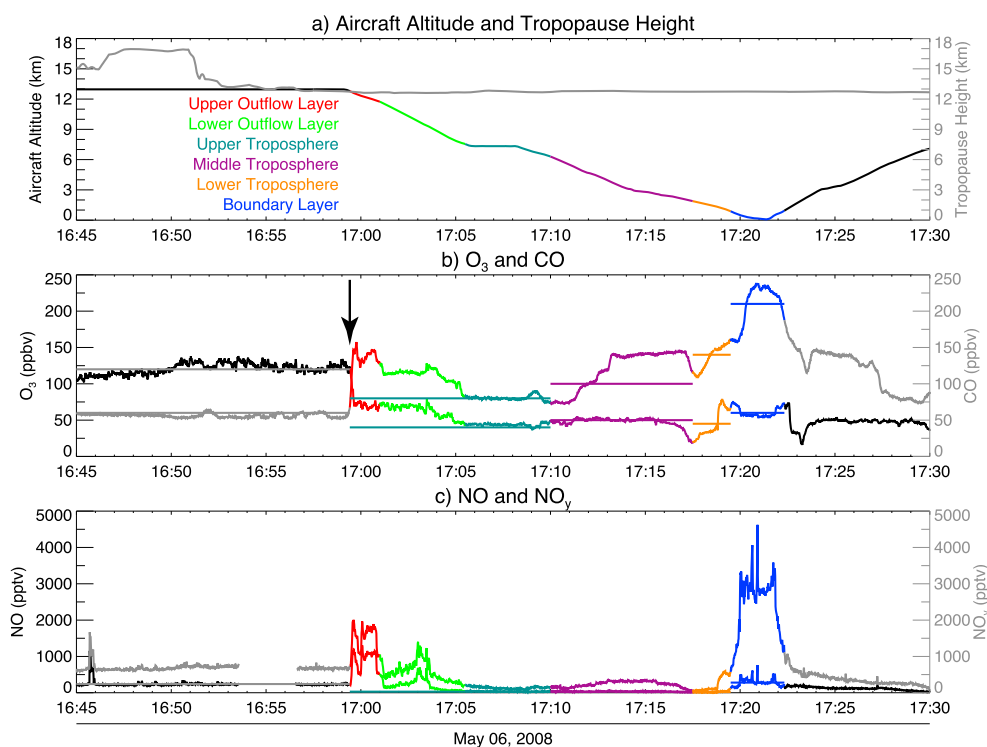


Figure 2. Measured parameters between the points labeled A and B in Figure 1. (a) Aircraft altitude (black plus colors) and tropopause height (gray); (b) ozone (black plus colors) and carbon monoxide (gray plus colors); (c) NO (black plus colors) and NO_y (gray plus colors). Various subjectively identified layers are color coded in all three panels. The Upper Troposphere layer is assumed to represent unperturbed background upper tropospheric air. The horizontal lines in Figures 2b and 2c are the representative values for each layer used to predict values in the upper (red) and lower (green) outflow layers in combination with the back trajectories. The values are tabulated in Table 3. Note that in Figure 2b, the O₃ and CO time series cross over each other near the tropopause, which is indicated by an arrow.

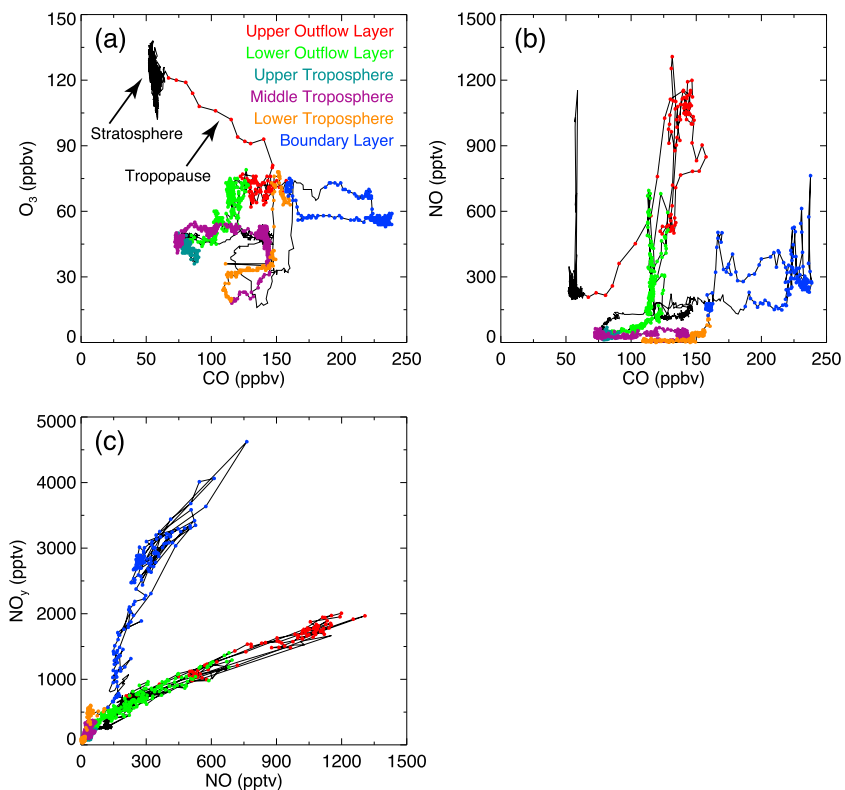


Figure 3. Tracer-tracer plots of (a) O_3 versus CO, (b) NO versus CO, and (c) NO_y versus NO for the period 16:45 UTC and 17:30 UTC, 6 May. The observations are color coded as in Figure 2. Stratosphere and tropopause are indicated in Figure 3a.

4. Results

4.1. START08 Research Flight 8

Research Flight 8 (RF08) took place on 6 May 2008 from 14:55 UTC until 21:32 UTC (Figure 1). The aircraft took off from Colorado and flew out over the Gulf of Mexico before returning to Colorado. The aircraft descended from the LS and executed a missed approach at Ponca City, OK. It then ascended once more into the LS, flew above a weakening squall line located in northern Texas and Oklahoma, and then descended to execute a second missed approach at Alexandria, LA (label 2 in Figure 1). The descent to the second missed approach provided a profile of the outflow from the squall line and the environment into which the squall line was propagating.

Several quantities observed by the aircraft during the squall line overflight and descent are plotted as a function of time in Figure 2. This portion of the flight occurs between 16:45 and 17:30 UTC and is the segment of the flight track between the labels A and B in Figure 1. Figure 2a shows the tropopause height at the aircraft location from the WRF analysis (gray) and the aircraft altitude (black plus colors). The colors indicate possible atmospheric layers identified subjectively based on the trace species profiles shown in Figures 2b and 2c.

The O_3 (black plus colors) and CO (gray plus colors) data show the descent from just above the tropopause into the troposphere near 16:59 UTC (Figure 2b). There is a transitional mixing layer approximately 150 m thick between the stratosphere and troposphere (12.786 to 12.632 km altitude or 184.1 to 188.8 hPa) within which O_3 and CO rapidly change from stratospheric to tropospheric values. The relationship between O_3 and CO is linear within the mixing layer (Figure 3a).

The NO and NO_y data in particular suggest the presence of two distinct outflow layers in the UT. These are colored red and green (Figure 2c). The upper layer includes the shallow stratosphere-troposphere transition layer and extends from 12.786 km to 11.739 km (~ 1.0 km from 184.1 to 217.5 hPa); the lower layer is deeper and extends from 11.739 to 7.542 km (~ 4.2 km from 217.5 to 399.7 hPa). For simplicity, in what follows we refer to these as the red and green layers, respectively. The NO and NO_y concentrations in the two outflow

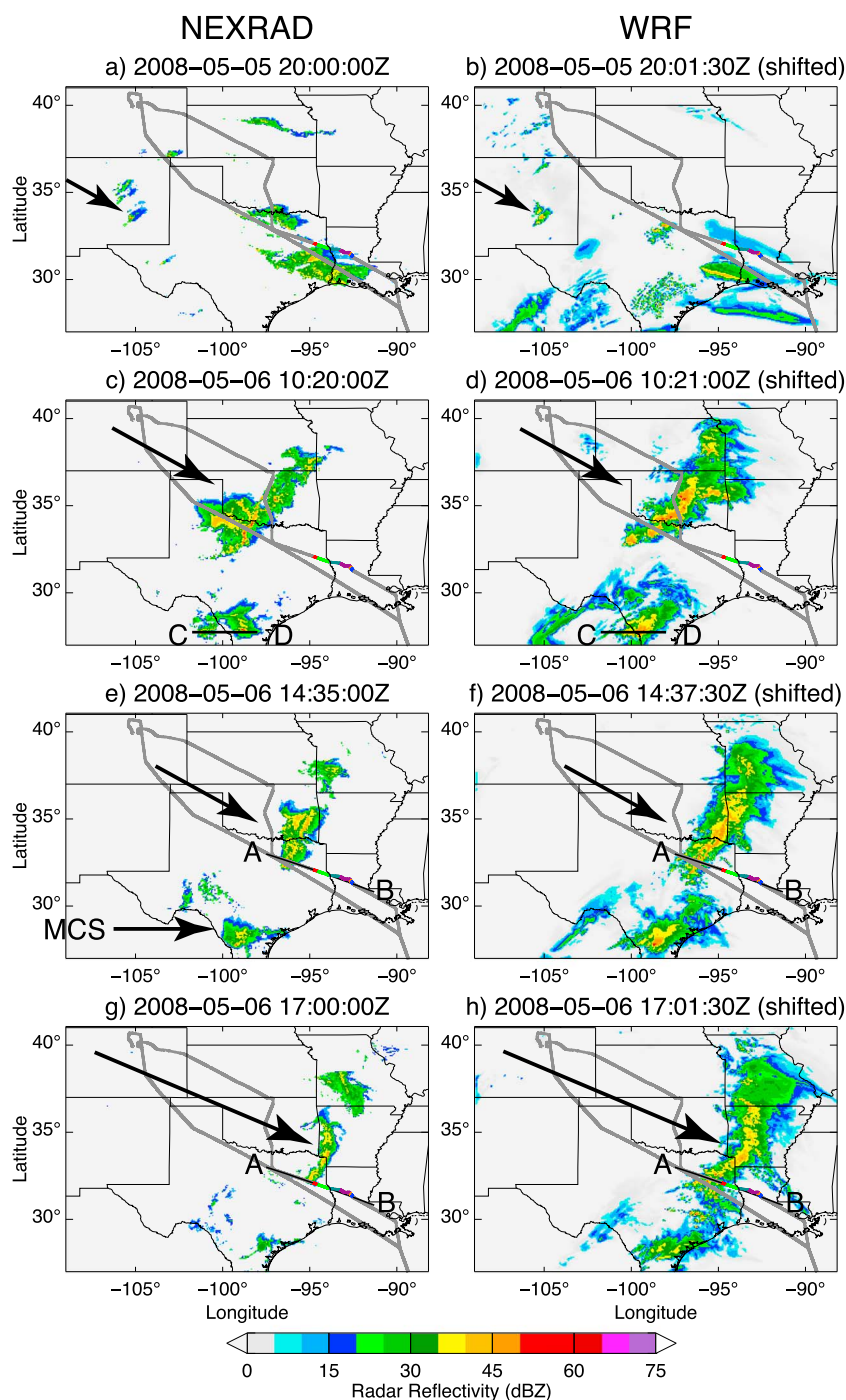


Figure 4. Maps showing the column-maximum observed and simulated radar reflectivity of the squall line at different stages (arrows). The time in the WRF simulation is shifted back by seven archival time steps (31.5 min). Vertical sections of the observed and simulated radar reflectivity along lines labeled A–B and lines labeled C–D are shown in Figures 5 and 13, respectively. Colors along the flight track indicate the layers as shown in Figure 2.

layers are much larger than those in the MT and LT. The observed NO concentration is also larger in the outflow layers than in the BL, which is sampled near 17:20 UTC, while the NO_y concentration is smaller than BL values.

The relationships between selected trace species during the time period of Figure 2 are shown in Figure 3. The color coding is the same as in Figure 2. The stratosphere has a distinct combination of high O₃ and low CO. The transition layer between the stratosphere and troposphere mentioned above is labeled “tropopause”

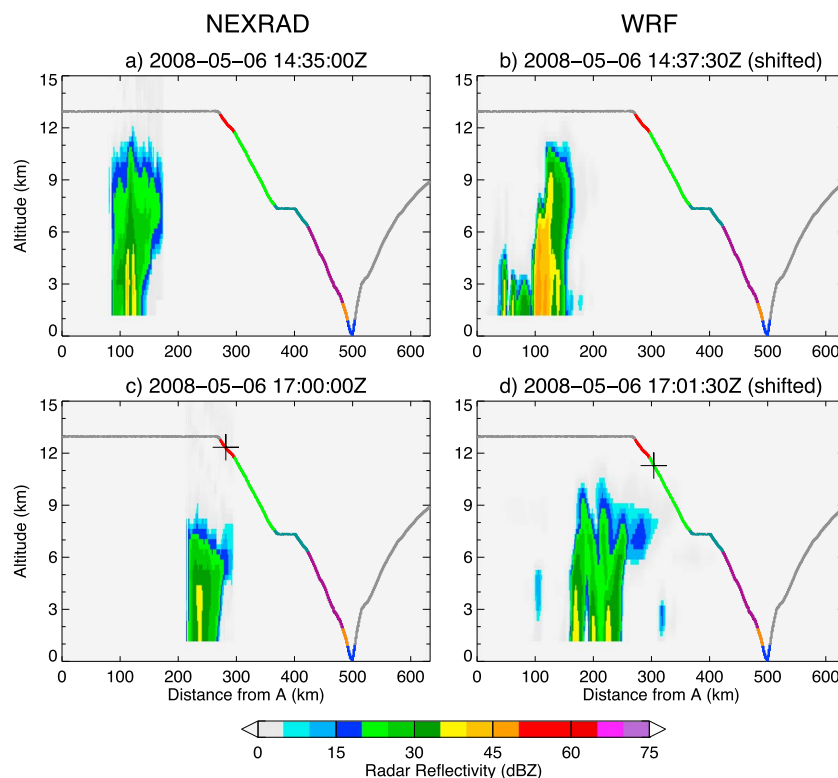


Figure 5. Vertical sections of the (a and c) observed and (b and d) simulated radar reflectivity along lines labeled A–B in Figures 4e–4h, respectively. The plus sign indicates the location of the aircraft. Colors along the flight track indicate the layers as shown in Figure 2. The time in WRF simulation is shifted back by seven archival time steps (31.5 min).

in Figure 3a. During this part of the flight, NO and NO_y exhibit nearly linear relationships within two different regimes, the BL and the rest of the atmosphere (Figure 3c), with the ratio of NO_y to NO being much larger in the BL as shown by *Ehhalt and Rohrer [1995]*. Other aspects of Figure 3 are discussed further below.

4.2. Evolution of the Squall Line

The evolution of the squall line system observed during RF08 can be seen in NEXRAD data (left) and the WRF simulation (right) (Figure 4). The convective system of interest is identified by arrows in each panel. The squall line starts as isolated convective cells on 5 May (Figure 4a). WRF produces similar isolated convection through the evening (Figure 4b). The isolated storm cells move eastward and begin to merge around 23:00 UTC. An organized squall line forms by 08:00 UTC, 6 May 2008.

A leading-line, trailing-stratiform (LLTS) MCS can be recognized with a northeast-southwest orientation and column maximum radar reflectivity at the leading edge exceeding 50 dBZ at 10:20 UTC 6 May 2008 (Figure 4c). The simulated squall line has a similar intensity and orientation but propagates slightly faster than its observed counterpart (Figure 4d). To improve the match between observation and simulation, we compare observations for a given time with the simulation from 31.5 min earlier, which is equivalent to seven archival time steps. There is also a nonsquall-line MCS moving eastward from northern Mexico to southern Texas (see label in Figure 4e).

At 14:35 UTC, the simulated squall line is somewhat stronger than the observations (Figures 4e and 4f). The aircraft flew just above the top of the outflow cirrus near 17:00 UTC on 6 May and then descended to make a missed approach in Louisiana near 17:21 UTC (Figure 4g). At the time of the overflight and descent, the simulated squall line is somewhat stronger than the observations, but the structure is similar (Figure 4h). After adjusting for the slightly faster propagation speed of the squall line in the simulation, we find the horizontal structure and location of the squall line in the WRF simulation to be consistent with the NEXRAD data.

Figure 5 shows vertical sections of the simulated and observed radar reflectivity approximately 2.5 h before and at the time of the aircraft overflight near the southern end of the squall line (line A–B in Figures 4e and 4f). Vertical sections taken at other locations are similar. In Figures 5c and 5d the location of the aircraft at

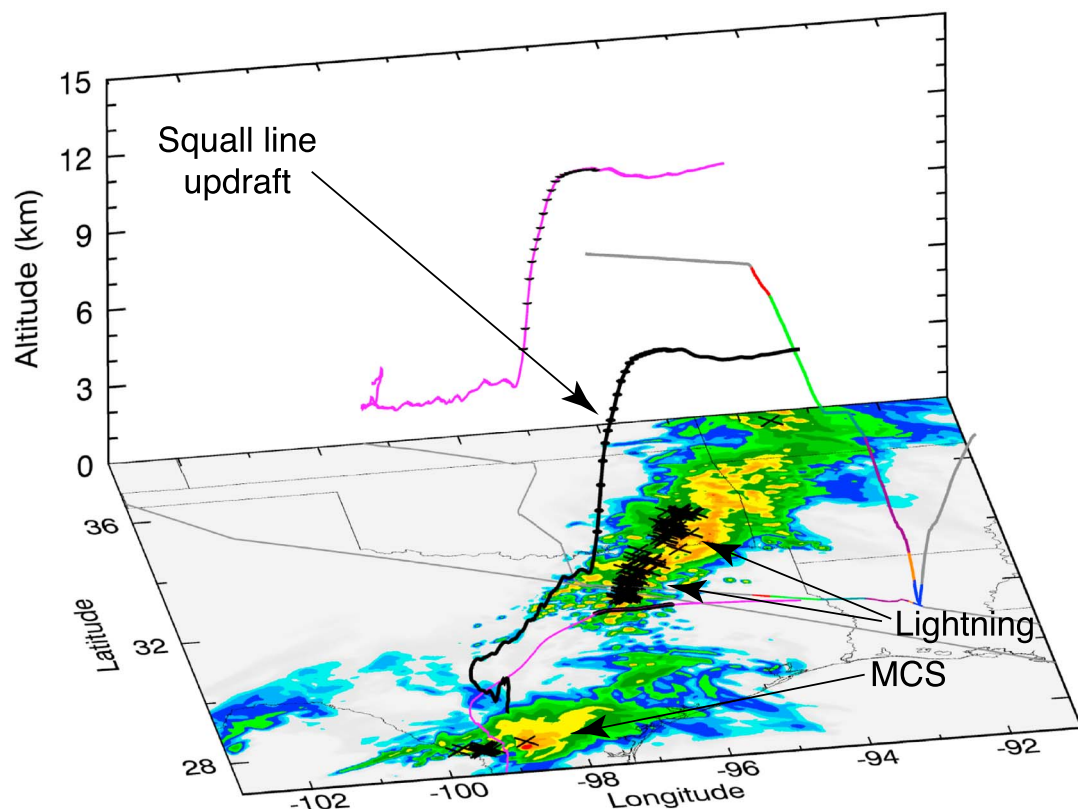


Figure 6. A typical 24 h back trajectory for air parcels convected by the squall line. The 3-D trajectory is shown in black; longitude-latitude and longitude-altitude projections of the trajectory are plotted in magenta. Near the time of the simulated radar map (14:15 UTC 6 May 2008) the parcels ascend rapidly in updrafts within the squall line. This interval is indicated by black dots plotted on the trajectories. Observed lightning flashes occurring near this time are indicated by black crosses superimposed on the radar map. The position of the MCS at this time is also indicated.

the respective time is indicated by a plus sign. At the earlier times the detectable echo tops reach near 11 km altitude (Figures 5a and 5b), which is the boundary between the green and red layers, using 15 dBZ as the threshold. As the squall line weakens the depth of the convection decreases, but the simulated squall line weakens more slowly and remains somewhat deeper and broader than the observations. The vertical sections suggest that the air in the green and red layers was transported to the upper troposphere several hours before it was observed by the aircraft. This is confirmed by the trajectory studies in the next section.

4.3. Trajectory Analysis

In order to determine the source regions of the air in the upper and lower outflow layers, back trajectories are computed for a three-dimensional grid of particles initialized in a rectangular volume surrounding the aircraft flight path.

4.3.1. Lower Outflow Layer

For the green layer the initial volume of particles lies between 93.9° and 94.5°W, 31.7° and 32.0°N, and $\eta = 0.3650$ and 0.18 (7.6 and 11.6 km). With a grid spacing of $0.1^\circ \times 0.1^\circ \times 0.0025 \eta$ (approximately 9.5 km \times 11 km \times 53 m in this part of UT), the volume for the green layer includes $7 \times 4 \times 75 = 2100$ particles.

Analysis of the back trajectories of the air in the green layer reveals that parcels arrive through three different pathways: 40% is convected to the UT by the squall line that the aircraft overflew immediately before descending through the outflow layer; 8% is convected by the MCS located in northern Mexico; and 52% is environmental air from the UT and MT.

Figure 6 shows a representative trajectory for a parcel convected by the squall line. For clarity, only a single trajectory is plotted. Other trajectories in this group are tightly bunched around this trajectory. Note that while the plotted trajectory shows many hours of motion by the parcel, the simulated radar map is for a single time,

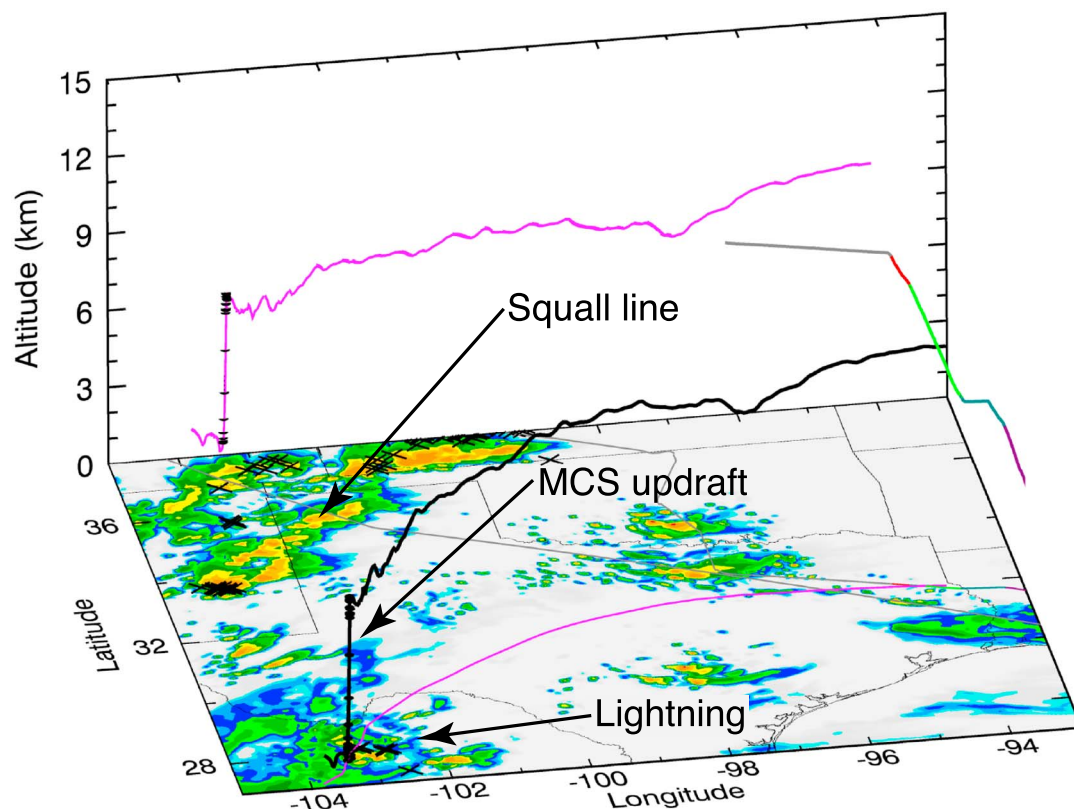


Figure 7. A typical 24 h back trajectory for air parcels convected by the southern MCS. The 3-D trajectory is shown in black; longitude-latitude and longitude-altitude projections of the trajectory are plotted in magenta. Near the time of the simulated radar map (00:00 UTC 6 May 2008) the parcels ascend rapidly in updrafts within the MCS. This interval is indicated by black dots plotted on the trajectories. Observed lightning flashes occurring near this time are indicated by black crosses superimposed on the radar map. The position of the squall line at this time is also indicated.

in this case for 14:15 UTC 6 May, which is during the interval when the parcels ascend rapidly in the updraft. The portion of the trajectory within ± 45 min of the radar time is indicated by black dots plotted along the trajectory. The parcels in this group come from the LT and MT in southern Texas and from the BL and LT in northern Mexico. After moving generally northward at low levels and northeastward at middle levels, they ascend to the UT in the updrafts near the southwestern end of the squall line. This occurs approximately 2.75 h before they reach the volume sampled by the aircraft near 17:00 UTC.

The second convective system responsible for transporting air to the green layer (8%) is the nonsquall MCS in northern Mexico. This system is seen in Figure 4 in both the NEXRAD data and the WRF simulation. This southern MCS moves eastward from northern Mexico to southern Texas and dies out around 18 UTC 6 May. Figure 7 shows a representative example for a parcel convected by the MCS. In this case the radar map is for 00:00 UTC 6 May, which is during the interval when the parcels are ascending rapidly in the updrafts. The parcels in this group come from northern Mexico and are initially located at levels from the BL to the MT. After ascending to the UT in the updrafts of the MCS, they move generally northeastward. This occurs approximately 17 h before the volume is sampled by the aircraft, which is 14 h before the convective transport by the squall line. There are some CG flashes in this MCS around 00:00 UTC 6 May (± 4.5 min).

The distributions of sources and transport pathways for parcels in the green layer are given in Figure 8 as a function of altitude. Parcels that are transported by the squall line (SQ, light red), southern MCS (MCS, light gray), and other (light blue) show that the two MCSs account for convecting more than 50% of parcels above 9.2 km (Figure 8a). The parcels can also be classified by their source regions. In Figure 8b, parcels that come from the UT, MT, LT, and BL are colored in dark green, purple, orange, and blue, respectively. At all levels the sources are dominated by air from the MT and LT.

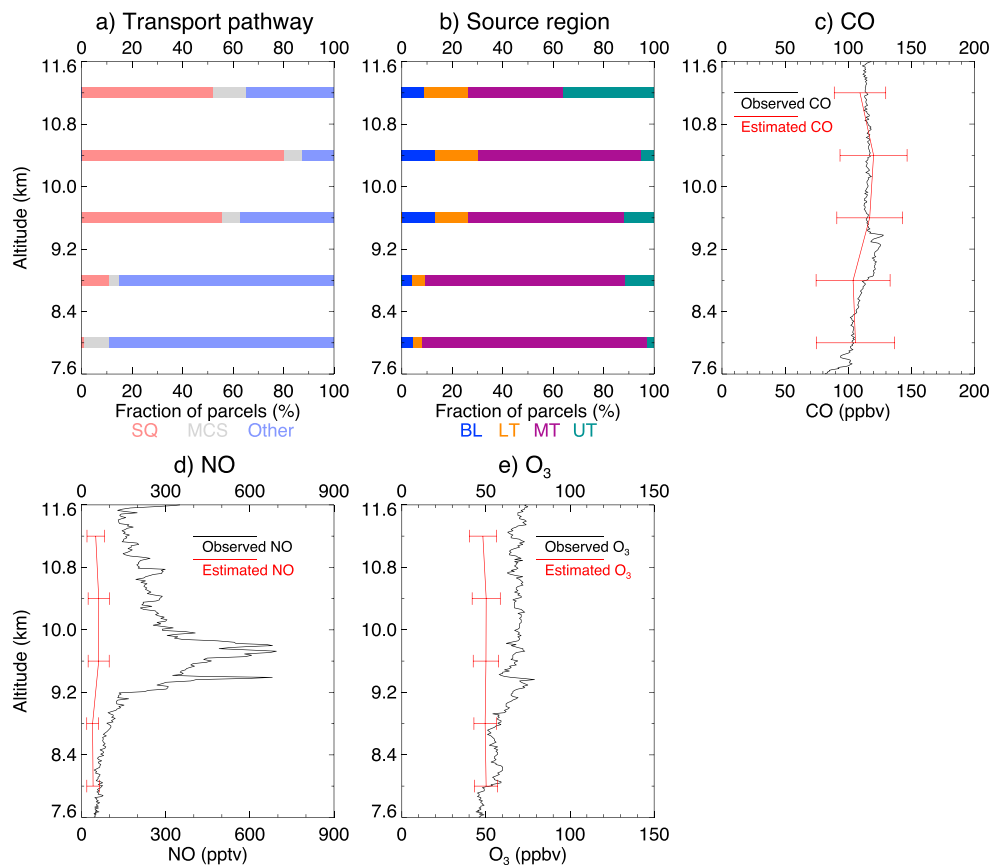


Figure 8. Lower (green) outflow layer as a function of altitude. (a) Fraction of parcels by transport pathway: squall line (light red), southern MCS (light gray), and other (light blue). (b) Fraction of parcels by source region: boundary layer (blue), lower troposphere (orange), middle troposphere (purple), and upper troposphere (dark green). (c) Concentration of CO. (d) Concentration of NO. (e) Concentration of O₃. In Figures 8c–8e, observations are black lines and estimates from the mixing model are red lines. Error bars indicate the uncertainty in estimates that is equivalent to $\pm 1 \sigma$ deviation.

Using equation (3) and the parcel source region fractions from Figure 8b, we estimate the concentrations of CO, NO, and O₃ as a function of altitude assuming that they are conserved. The values used as the initial concentrations in the source regions are plotted as horizontal lines on the aircraft time series in Figures 2b and 2c. These values and their uncertainties, which are estimated from the variability of the various species within each source region, are given in Table 3. The geographical region sampled is the portion of the flight path between the labels A and B in Figure 1. The assumption that the trace species concentrations in the layers are horizontally homogeneous can be evaluated to some extent by comparing the additional profiles collected on the flight in Louisiana and over the Gulf of Mexico (2–3, 4–5, and 5–6) in Figure 1. Figure 9 shows that in general the concentrations of O₃, CO, NO, and NO_y are quite similar in all of the profiles, which supports

Table 3. Means and Standard Deviations of the Mixing Ratios of CO, NO, and O₃ in Each of the Source Layers Used With the Trajectories to Predict the Measured Values

Source Region	CO (ppbv)		NO (pptv)		O ₃ (ppbv)	
	Mean	S.D.	Mean	S.D.	Mean	S.D.
Lower stratosphere (LS)	60	4.5	240	79.8	120	7.5
Upper troposphere (UT)	80	3.3	30	9.3	40	2.4
Middle troposphere (MT)	100	32.9	30	11.7	50	7.1
Lower troposphere (LT)	140	17.4	20	23.2	45	18.9
Boundary layer (BL)	210	28.4	280	104.3	60	6.8

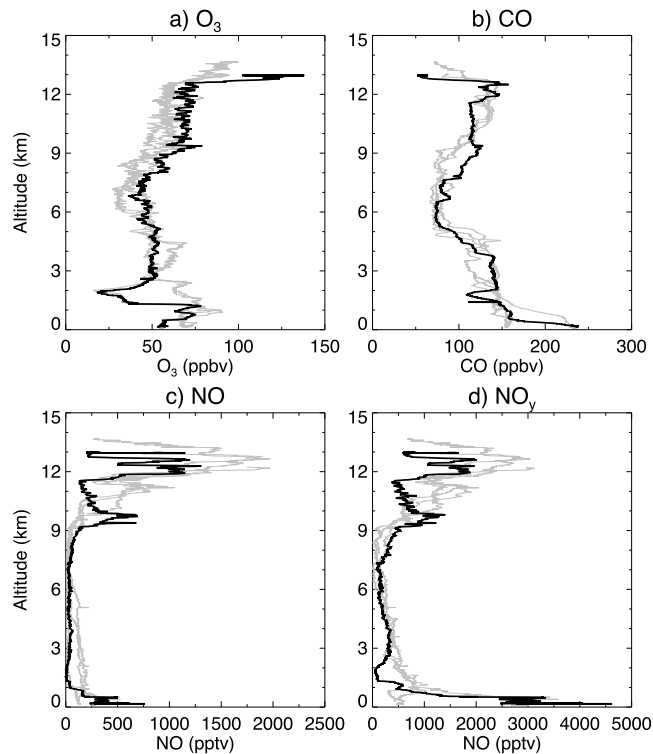


Figure 9. Deep profiles from Research Flight 8 as a function of altitude. (a) Concentration of O_3 ; (b) concentration of CO; (c) concentration of NO; and (d) concentration of NO_y . Black line: primary profile, 1–2 in Figure 1. Gray lines: additional profiles, 2–3, 4–5, and 5–6 in Figure 1.

the assumption of horizontal homogeneity in the mixing model. Unfortunately, no observations are available from the area of the MCS, so we use the observations from the RF08 flight path in all of the calculations.

The values of CO, NO, and O_3 predicted by the mixing model, and their uncertainties for each of the five layers, are plotted with red lines in Figures 8c–8e, respectively. The estimated and observed CO concentrations agree well and are nearly constant in the vertical within the green layer. The estimated NO concentration agrees well at lower levels, but the model fails to reproduce the broad peak in NO in the upper and middle of the layer between 8.8 and 11.2 km. The estimated O_3 concentration also agrees well at lower levels, but not in the

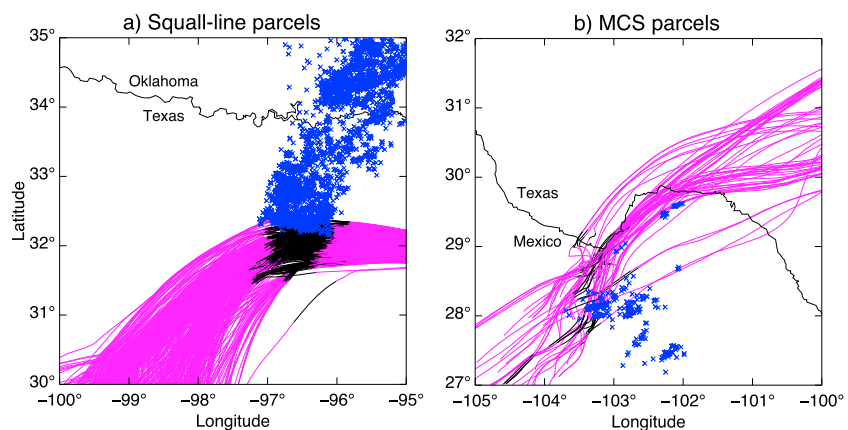


Figure 10. Expanded maps of parcel trajectories that are convected to the lower outflow layer by (a) the squall line and (b) the MCS. The black segments of the parcel tracks indicate the convective updrafts. Blue crosses are the locations of lightning flashes. In Figure 10a, the trajectories reach 8.8 to 11.2 km in the lower outflow layer. Lightning flashes are for the period from 13:30 to 15:00 UTC on 6 May 2008. In Figure 10b, the trajectories reach 7.6 to 9.4 km. Lightning flashes are for the period from 23:15 UTC on 5 May 2008 to 00:45 UTC on 6 May 2008.

Table 4. Comparison of Key Parameters in Equation (1) From the Field Campaigns START08, TROCCINOX, and AMMA^a

Field Campaign (latitude)	χ_{LNO_x} (ppbv)	ρ_a (kg m ⁻³)	$ \vec{V}_a - \vec{V}_s $ (m s ⁻¹)	Δx (km)	Δz (km)	F_{LNO_x} (g s ⁻¹)	P_{LNO_x} (mol flash ⁻¹)
START08 (26°–41°N)	~0.25	~0.4	~20	~380	~2.4	880	31
TROCCINOX (19°–22°S)	0.1–1.1	0.36–0.41	5–15	~30–50	~3–4	48–178	71–200
AMMA (9°–15°N)	0.2	0.33–0.36	7–9	~150–220	~2–3	85–135	71–179

^aThe values of parameters in TROCCINOX and AMMA are extracted from Huntrieser *et al.* [2008, 2011].

upper and middle parts of the green layer. This sublayer also shows up distinctly in the scatterplots (Figures 3a and 3b). It is unlikely that the peak in NO and the elevated O₃ are due to transport from the BL, because CO remains constant in this layer. If the air came from the BL, then CO should increase along with NO and O₃. We note instead that at the time the parcels ascend in the updrafts, lightning occurs in the squall line, indicated by black crosses in Figure 6. An expanded map of the region (Figure 10a) near the squall line updrafts in Figure 6 shows all of the trajectories between 8.8 and 11.2 km along with observed CG flashes occurring while the parcels were in the updrafts (13:30 UTC to 15:00 UTC). An expanded map of the region (Figure 10b) near the MCS updrafts in Figure 7 shows all of the trajectories between 7.6 and 9.4 km along with observed CG flashes occurring while the parcels were in the updrafts (13:30 UTC to 15:00 UTC). While there are only a few CG flashes associated with the convection in the southern MCS case when these parcels were ascending in the updrafts, it is possible that there is substantial intracloud (IC) lightning occurring at this time. On the contrary, the small

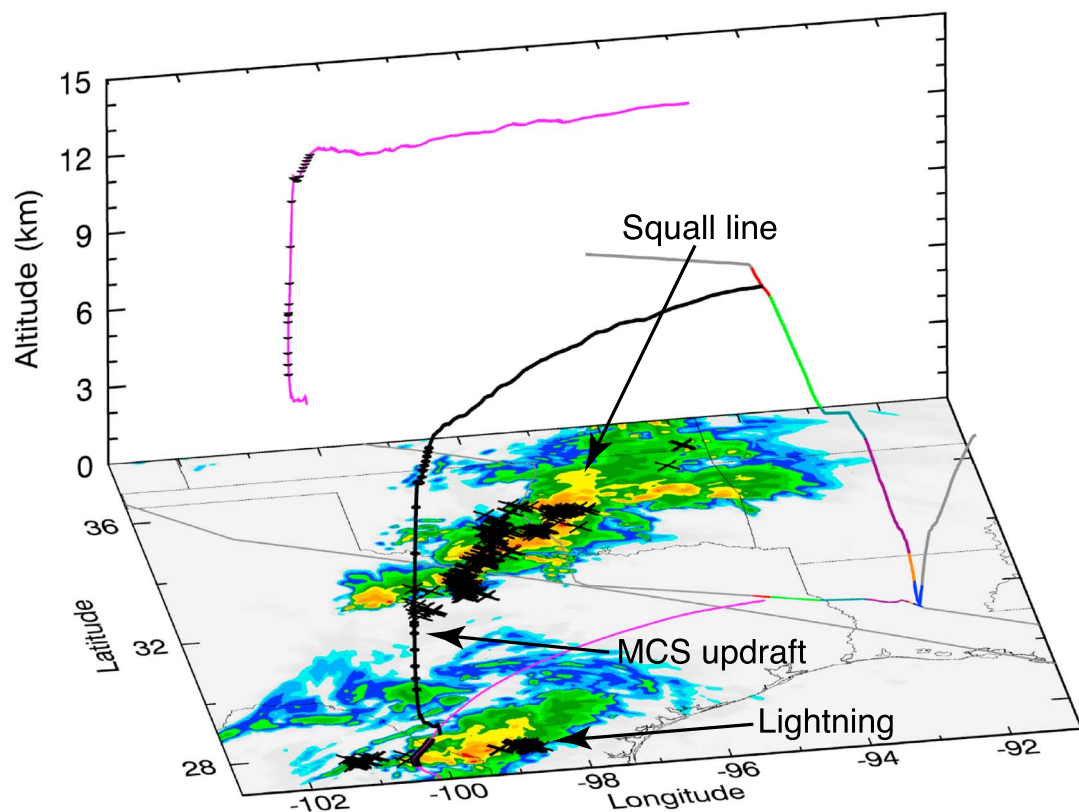


Figure 11. A typical 24 h back trajectory for air parcels convected by the southern MCS. The 3-D trajectory is shown in black; longitude-latitude and longitude-altitude projections of the trajectory are plotted in magenta. Near the time of the simulated radar map (10:21 UTC 6 May 2008) the parcels ascend rapidly in updrafts within the MCS. This interval is indicated by black dots plotted on the trajectories. Observed lightning flashes occurring near this time are indicated by black crosses superimposed on the radar map. The position of the squall line at this time is also indicated.

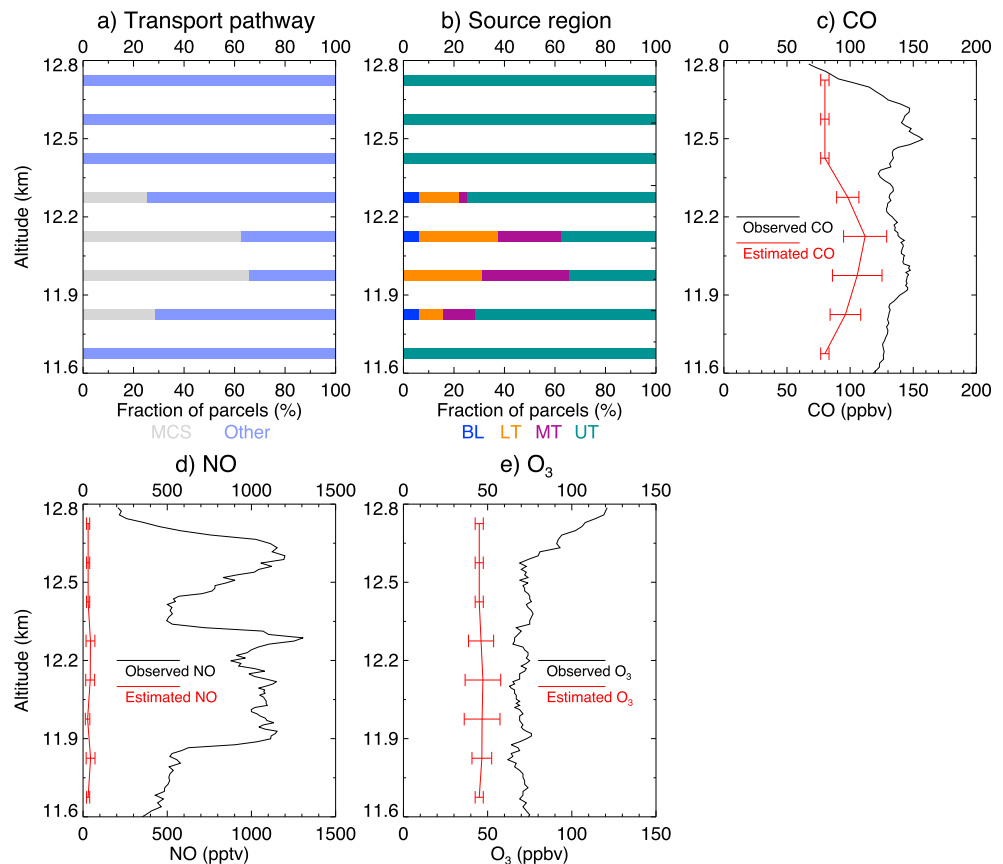


Figure 12. Upper (red) outflow layer as a function of altitude. (a) Fraction of parcels by transport pathway: southern MCS (light gray), and other (light blue). (b) Fraction of parcels by source region: boundary layer (blue), lower troposphere (orange), middle troposphere (purple), and upper troposphere (dark green). (c) Concentration of CO. (d) Concentration of NO. (e) Concentration of O₃. In Figures 12c–12e, observations are black lines and estimates from the mixing model are red lines. Error bars indicate the uncertainty in estimates that is equivalent to $\pm 1 \sigma$ deviation.

number of CG flashes may account for the smaller difference between observed and predicted values of NO below 9.2 km.

In the squall line case, we estimate the production rate of LNO_x per flash (P_{LNO_x}) by first calculating the amount of horizontal LNO_x mass flux using equation (1). The key parameters in the equation are given in Table 4. Same parameters from the other field campaigns (Tropical Convection, Cirrus and Nitrogen Oxides Experiment (TROCCINOX, Brazil) and African Monsoon Multidisciplinary Analysis (AMMA, West Africa)) are also included for comparison because they also estimate the P_{LNO_x} of subtropical and tropical MCSs. The outflow region is estimated to be between 9.2 and 11.6 km (Figure 8a). This range is used to estimate the mean NO_x volume mixing ratio produced by lightning (χ_{LNO_x}) and the mean air density at the outflow region (ρ_a). Since the difference of wind direction between the horizontal wind velocity in the anvil (\vec{V}_a , $\sim 30 \text{ m s}^{-1}$) and the wind velocity of the squall line (\vec{V}_s , $\sim 10 \text{ m s}^{-1}$ at 700 hPa) is very small ($\sim 10^\circ$), we assume that they blow at the same direction. The production rate of LNO_x per flash is then calculated using equation (2). Since the NLDN CG flash rate is $\sim 0.5 \text{ flash s}^{-1}$ during the time of updraft and the ratio of IC to CG lightning is assumed to be 3 to 1, the NLDN total flash rate (R_{NLDN}) is estimated to be $\sim 2 \text{ flash s}^{-1}$. The P_{LNO_x} value is $\sim 31 \text{ mol flash}^{-1}$. Huntrieser *et al.* [2008] report the relative error in their estimate of the horizontal mass flux of LNO_x from the anvil to be 190%. In this case we have slightly better estimates of some parameters, such as the depth of the outflow layer, but worse estimates of others, such as the length of the squall line, and estimate the error to be of similar magnitude ($\sim 200\%$).

4.3.2. Upper Outflow Layer

For the red layer the initial volume of particles lies between 94.6° and 94.9°W , 31.9° and 32.2°N , and $\eta = 0.1775$ and 0.14 (11.6 and 12.8 km). With a grid spacing of $0.1^\circ \times 0.1^\circ \times 0.0025 \eta$ (approximately $9.5 \text{ km} \times 11 \text{ km} \times 75 \text{ m}$ in this part of UT), the volume for the red layer includes $4 \times 4 \times 16 = 256$ particles.

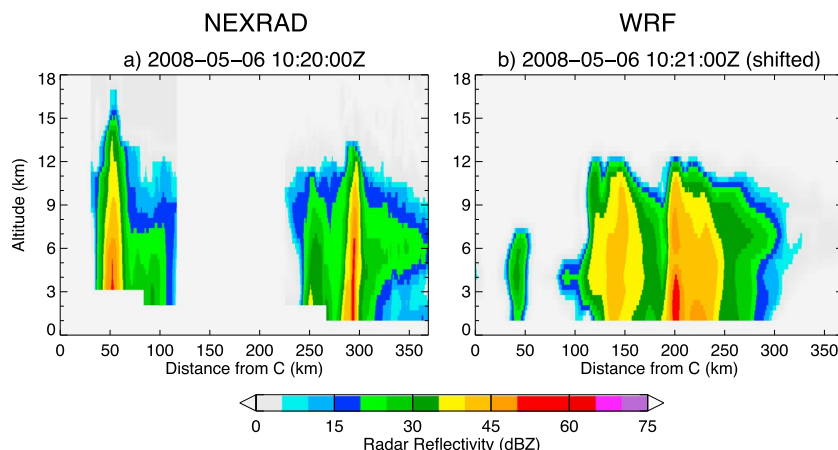


Figure 13. Vertical sections of the (a) observed and (b) simulated radar reflectivity along lines labeled C–D in Figures 4c and 4d, respectively. The time in WRF simulation is shifted back by seven archival time steps (31.5 min).

Analysis of the back trajectories of the air in the red layer reveals that parcels arrive through two different pathways: 23% is convected to the UT by the MCS located in southern Texas that also contributed to the green layer, and 77% is environmental air from the LS and UT. Figure 11 shows a representative trajectory for a parcel convected by the MCS. The simulated radar map is for 10:21 UTC 6 May. The portion of the trajectory within ± 45 min of the radar time is indicated by black dots plotted along the trajectory. The parcels in this group come from northern Mexico and southern Texas and are initially located at levels from the BL to the MT. After ascending to the UT in the updrafts of the MCS, they move generally northeastward. This occurs approximately 6.5 h before the volume is sampled by the aircraft. Although the MCS responsible for this air is the same as that in Figure 6, the northeastward transport occurs more rapidly at the higher altitudes due to vertical shear in the large-scale horizontal wind.

The distributions of sources and transport pathways for parcels in the upper (red) layer are given in Figure 12 as a function of altitude. Parcels transported by the MCS (light gray) account for more than 50% of the parcels between 11.9 and 12.2 km (Figure 12a). In Figure 12b it can be seen that all of the parcels transported by the MCS come from the BL, LT, and MT. All of the remaining parcels (light blue) come from the UT. Predicted concentrations of CO, NO, and O₃ as a function of altitude in the red layer are plotted in Figures 12c–12e along with the observations. The predicted CO concentration is somewhat low in the lower part of the layer (>12.4 km), while the difference is larger in the upper part of the layer (<12.4 km). The predicted NO and O₃ concentrations are lower than observations throughout the layer, and the mixing model does not capture the minimum in NO near 12.4 km.

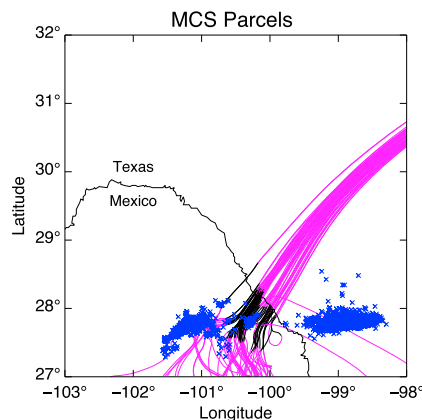


Figure 14. Expanded map of parcel trajectories that are convected to the upper outflow layer by the southern MCS. The black segments of the parcel tracks indicate the convective updrafts. Blue crosses are the locations of lightning flashes. The trajectories reach 11.8 to 12.4 km in the upper outflow layer. Lightning flashes are for the period from 09:36 to 11:06 UTC on 6 May 2008.

The parcel trajectories indicate that air in the upper part of the red layer is entirely from the upper troposphere, but the observed CO and NO are near 140 ppbv and >1200 pptv, respectively. Figure 13 shows vertical sections of the simulated and observed radar reflectivity of the MCS at the time of the convective transport (Figure 11) along the lines labeled C–D in Figures 4c and 4d. Although the simulated MCS appears somewhat larger and more intense than the observed (Figures 4c and 4d), the observed echo tops reach 15 km, while those in the model reach only to 12 km, which is about the same height as the peak of convection in Figure 12a. These results together suggest that the convective transport to the red layer as a whole is underestimated by the model because the model convection does not extend quite high enough (up to 12.4 km in Figure 12b). The result is a large underprediction of CO in the upper part of the layer and NO in the whole layer. This is different from the green layer, where the observed and simulated squall lines have similar intensities and echo top heights and the concentrations are well predicted by the trajectories and simple mixing model. For the red layer it might also be the case that we underestimate the CO concentrations in the middle and lower tropospheric source regions due to inadequate sampling of the source regions by the aircraft.

At lower levels within this layer, where a substantial fraction of the air parcels come from the MT, LT, and BL, predicted CO is low by 15 to 30%, while O₃ is low by 40%. NO, on the other hand, is low by a factor of 20. The large NO discrepancy is likely due to lightning sources. Lightning is observed to occur during the time period these parcels ascend in the updrafts of the southern MCS from an expanded map of the region (Figure 14) near the updrafts in Figure 11.

5. Conclusions

This study attempts to determine the origin and transport pathways of air in the upper tropospheric outflow from a squall line observed in northern Texas during the START08 field program. The outflow air, which is located in the top few kilometers of the troposphere, is characterized by two distinct layers with high values of CO and NO/NO_y. Air parcel trajectories for the observed outflow layers are computed using three-dimensional wind fields from a high-resolution simulation with the Weather Research and Forecasting (WRF) model. The model is initialized more than a day prior to the time the aircraft observations were made and is integrated forward using initial and boundary conditions taken from operational analyses. The model reproduces the initiation, growth, and decay phases of the observed convective systems with good fidelity. The primary differences between the model and observations are that the simulated squall line propagates eastward slightly faster and weakens more slowly during the later stages than is observed.

Back trajectories computed with the WRF wind fields show that the air in the outflow layers is a mixture of air parcels with sources ranging from the boundary layer to the upper troposphere. The trajectories also show that significant contributions to the outflow air come not only from the nearby squall line but also from a nonsquall-line MCS located in northern Mexico and southern Texas. One of the limitations of this study is the lack of observations in all of the source regions.

In the lower (green) outflow layer, 52% of the air parcels are environmental air from the middle and upper troposphere, while 40% and 8% of the parcels, respectively, are transported vertically by convection within the squall line and MCS. The observed concentrations of CO, NO, and O₃ in the lower outflow layer are predicted as a function of altitude using a simple mixing model based on the observed aircraft profiles of CO, NO, and O₃ and the contributions from different source altitudes estimated from the back trajectories. The model, which assumes that CO, NO, and O₃ are conserved during transport, captures the vertical profile of CO throughout the lower outflow layer and of NO and O₃ at the bottom and top of the layer, but fails to reproduce the enhanced NO and O₃ in the upper part of the layer. The average NO concentration predicted by the mixing model in the upper part of the layer (above 9.2 km) is ~60 pptv, while the average of the observed values is ~280 pptv, which implies that ~80% of the NO in that part of the layer is produced by lightning. Data from the NLDN show that lightning was occurring at the time air parcels were transported vertically by the squall line to the altitude of the lower outflow layer. Assuming that all of the NO above 9.2 km is produced by the lightning in the squall line, on average 31 moles of NO per IC/CG flash are needed to match the observation.

In the upper (red) outflow layer, 23% of the particles are transported from the MCS and the remaining 77% are environmental air from the LS and UT. Although the upper outflow layer is immediately downwind of the squall line system, the convective transport to this layer did not occur within the squall line but happened instead in the updrafts of the MCS in northern Mexico and southern Texas. This air then moved northward with the large-scale flow to produce the upper outflow layer. In the upper outflow layer the model underestimates

CO by 15 to 30% and NO by as much as a factor of 20. The discrepancies in the upper outflow layer appear to be largely due to an underestimate of the vertical transport to the upper part of the layer by the MCS and to the lack of a lightning source for NO. Based on these results we conclude that essentially all of the NO in the uppermost layer is produced by lightning.

These results demonstrate that high-resolution simulations of convective events can be used to interpret high-resolution in situ observations of important trace gases in terms of transport pathways and sources, such as lightning. With better information on the composition of the source regions, more sophisticated chemistry models could be used in either Eulerian or Lagrangian frameworks for post flight analysis. With current modeling capabilities it should also be possible to carry out high-resolution convective forecasts and trajectory calculations with sufficient lead time to plan aircraft flight paths to sample both inflow and outflow regions of targeted convective systems.

Acknowledgments

This research is funded by National Science Foundation grant AGS-1016191 to Texas A&M University. The authors wish to thank all of the producers, archivers, and distributors of the data and models used in the study. We thank Cameron Homeyer for processing 3-D gridded NEXRAD radar reflectivity composites. The START08 data (http://data.eol.ucar.edu/master_list/?project=START08) were obtained from the Earth Observing Laboratory at the National Center for Atmospheric Research (NCAR). NCAR is sponsored by the National Science Foundation. The radar data were obtained from the NEXRAD Data Archive at the NOAA National Climatic Data Center (<https://www.ncdc.noaa.gov/nexradinv/>). The Weather Research and Forecasting Model (WRF) is supported and distributed by the NCAR Mesoscale and Microscale Meteorology Division (<http://www.mmm.ucar.edu/wrf/users>). The WRF simulation output files can be obtained from the authors upon request. The NLDN data can be purchased from Vaisala (<http://forms.vaisala.com/webcontactwea>).

References

- Barth, M. C., et al. (2007), Cloud-scale model intercomparison of chemical constituent transport in deep convection, *Atmos. Chem. Phys.*, 7(18), 4709–4731, doi:10.5194/acp-7-4709-2007.
- Beljaars, A. C. M. (1995), The parametrization of surface fluxes in large-scale models under free convection, *Q. J. R. Meteorol. Soc.*, 121(522), 255–270, doi:10.1002/qj.49712152203.
- Bertram, T. H., et al. (2007), Direct measurements of the convective recycling of the upper troposphere, *Science*, 315(5813), 816–820, doi:10.1126/science.1134548.
- Boccippio, D. J., K. L. Cummins, H. J. Christian, and S. J. Goodman (2001), Combined satellite- and surface-based estimation of the intracloud cloud-to-ground lightning ratio over the continental United States, *Mon. Weather Rev.*, 129(1), 108–122, doi:10.1175/1520-0493(2001)129<0108:CSASBE>2.0.CO;2.
- Bowman, K. P. (1993), Large-scale isentropic mixing properties of the Antarctic polar vortex from analyzed winds, *J. Geophys. Res.*, 98(D12), 23,013–23,027, doi:10.1029/93JD02599.
- Bowman, K. P., and G. D. Carrie (2002), The mean-meridional transport circulation of the troposphere in an idealized GCM, *J. Atmos. Sci.*, 59(9), 1502–1514, doi:10.1175/1520-0469(2002)059<1502:TMMTCO>2.0.CO;2.
- Bowman, K. P., J. C. Lin, A. Stohl, R. Draxler, P. Konopka, A. Andrews, and D. Brunner (2013), Input data requirements for Lagrangian trajectory models, *Bull. Am. Meteorol. Soc.*, 94(7), 1051–1058, doi:10.1175/BAMS-D-12-00076.1.
- Bradshaw, J., D. Davis, G. Grodzinsky, S. Smyth, R. Newell, S. Sandholm, and S. Liu (2000), Observed distributions of nitrogen oxides in the remote free troposphere from the NASA Global Tropospheric Experiment Programs, *Rev. Geophys.*, 38(1), 61–116, doi:10.1029/1999RG900015.
- Chameides, W. L., D. D. Davis, J. Bradshaw, M. Rodgers, S. Sandholm, and D. B. Bai (1987), An estimate of the NO_x production rate in electrified clouds based on NO observations from the GTE/CITE 1 fall 1983 field operation, *J. Geophys. Res.*, 92(D2), 2153–2156, doi:10.1029/JD092iD02p02153.
- Chou, M.-D., and M. J. Suarez (1994), An efficient thermal infrared radiation parameterization for use in general circulation models, *NASA Tech. Memo. 104606*, Goddard Space Flight Center, Greenbelt, Md.
- Crum, T. D., R. L. Albery, and D. W. Burgess (1993), Recording, archiving, and using WSR-88D data, *Bull. Am. Meteorol. Soc.*, 74(4), 645–653, doi:10.1175/1520-0477(1993)074<0645:RAAUWD>2.0.CO;2.
- Crutzen, P. J., and J. Lelieveld (2001), Human impacts on atmospheric chemistry, *Annu. Rev. Earth Planet. Sci.*, 29(1), 17–45, doi:10.1146/annurev.earth.29.1.17.
- DeCaria, A. J., K. E. Pickering, G. L. Stenchikov, J. R. Scala, J. L. Stith, J. E. Dye, B. A. Ridley, and P. Laroche (2000), A cloud-scale model study of lightning-generated NO_x in an individual thunderstorm during STERAO-A, *J. Geophys. Res.*, 105(D9), 11,601–11,616, doi:10.1029/2000JD900033.
- Dickerson, R. R., et al. (1987), Thunderstorms: An important mechanism in the transport of air pollutants, *Science*, 235(4787), 460–465, doi:10.1126/science.235.4787.460.
- Dye, J. E., et al. (2000), An overview of the stratospheric-tropospheric experiment: Radiation, Aerosols, and Ozone (STERAO)-deep convection experiment with results for the July 10, 1996 storm, *J. Geophys. Res.*, 105(D8), 10,023–10,045, doi:10.1029/1999JD901116.
- Ehhalt, D. H., and F. Rohrer (1995), The impact of commercial aircraft on tropospheric ozone, in *The Chemistry of the Atmosphere—Oxidants and Oxidation in the Earth's Atmosphere: Proceedings of the 7th BOC Priestley Conference*, edited by A. R. Bandy, pp. 105–120, R. Soc. Chem., Lewisburg, Pa.
- Gerbig, C., S. Schmitgen, D. Kley, A. Volz-Thomas, K. Dewey, and D. Haaks (1999), An improved fast-response vacuum-UV resonance fluorescence CO instrument, *J. Geophys. Res.*, 104(D1), 1699–1704, doi:10.1029/1998JD100031.
- Homeyer, C. R. (2014), Formation of the enhanced-V infrared cloud-top feature from high-resolution three-dimensional radar observations, *J. Atmos. Sci.*, 71(1), 332–348, doi:10.1175/JAS-D-13-079.1.
- Homeyer, C. R., K. P. Bowman, and L. L. Pan (2010), Extratropical tropopause transition layer characteristics from high-resolution sounding data, *J. Geophys. Res.*, 115, D13108, doi:10.1029/2009JD013664.
- Hong, S.-Y., Y. Noh, and J. Dudhia (2006), A new vertical diffusion package with an explicit treatment of entrainment processes, *Mon. Weather Rev.*, 134(9), 2318–2341, doi:10.1175/MWR3199.1.
- Huntrieser, H., U. Schumann, H. Schlager, H. Höller, A. Giez, H.-D. Betz, D. Brunner, C. Forster, O. Pinto Jr., and R. Calheiros (2008), Lightning activity in Brazilian thunderstorms during TROCCINOX: Implications for NO_x production, *Atmos. Chem. Phys.*, 8(4), 921–953, doi:10.5194/acp-8-921-2008.
- Huntrieser, H., H. Schlager, M. Lichtenstern, P. Stock, T. Hamburger, H. Höller, K. Schmidt, H.-D. Betz, A. Ulanovsky, and F. Ravegnani (2011), Mesoscale convective systems observed during AMMA and their impact on the NO_x and O₃ budget over West Africa, *Atmos. Chem. Phys.*, 11(6), 2503–2536, doi:10.5194/acp-11-2503-2011.
- Jaeglé, L. (2007), Pumping up surface air, *Science*, 315(5813), 772–773, doi:10.1126/science.1138988.
- Jaeglé, L., et al. (1997), Observed OH and HO₂ in the upper troposphere suggest a major source from convective injection of peroxides, *Geophys. Res. Lett.*, 24(24), 3181–3184, doi:10.1029/97GL03004.

- Janjić, Z. I. (1994), The step-mountain Eta coordinate model: Further developments of the convection, viscous sublayer, and turbulence closure schemes, *Mon. Weather Rev.*, *122*(5), 927–945, doi:10.1175/1520-0493(1994)122<0927:TSMECM>2.0.CO;2.
- Lacis, A. A., D. J. Wuebbles, and J. A. Logan (1990), Radiative forcing of climate by changes in the vertical distribution of ozone, *J. Geophys. Res.*, *95*(D7), 9971–9981, doi:10.1029/JD095iD07p09971.
- Lelieveld, J., and P. J. Crutzen (1994), Role of deep cloud convection in the ozone budget of the troposphere, *Science*, *264*(5166), 1759–1761, doi:10.1126/science.264.5166.1759.
- Liu, S. C., D. Kley, M. McFarland, J. D. Mahlman, and H. Levy (1980), On the origin of tropospheric ozone, *J. Geophys. Res.*, *85*(C12), 7546–7552, doi:10.1029/JC085iC12p07546.
- Logan, J. A. (1983), Nitrogen oxides in the troposphere: Global and regional budgets, *J. Geophys. Res.*, *88*(C15), 10,785–10,807, doi:10.1029/JC088iC15p10785.
- Mlawer, E. J., S. J. Taubman, P. D. Brown, M. J. Iacono, and S. A. Clough (1997), Radiative transfer for inhomogeneous atmospheres: RRTM, a validated correlated-k model for the longwave, *J. Geophys. Res.*, *102*(D14), 16,663–16,682, doi:10.1029/97JD00237.
- Orville, R. E. (2008), Development of the National Lightning Detection Network, *Bull. Am. Meteorol. Soc.*, *89*(2), 180–190, doi:10.1175/BAMS-89-2-180.
- Orville, R. E., G. R. Huffines, W. R. Burrows, and K. L. Cummins (2011), The North American Lightning Detection Network (NALDN)—Analysis of flash data: 2001–09, *Mon. Weather Rev.*, *139*(5), 1305–1322, doi:10.1175/2010MWR3452.1.
- Pan, L. L., et al. (2010), The Stratosphere-Troposphere Analyses of Regional Transport 2008 (START08) experiment, *Bull. Am. Meteorol. Soc.*, *91*(3), 327–342, doi:10.1175/2009BAMS2865.1.
- Pickering, K. E., A. M. Thompson, R. R. Dickerson, W. T. Luke, D. P. McNamara, J. P. Greenberg, and P. R. Zimmerman (1990), Model calculations of tropospheric ozone production potential following observed convective events, *J. Geophys. Res.*, *95*(D9), 14,049–14,062, doi:10.1029/JD095iD09p14049.
- Poulida, O., R. R. Dickerson, and A. Heymsfield (1996), Stratosphere-troposphere exchange in a midlatitude mesoscale convective complex: 1. Observations, *J. Geophys. Res.*, *101*(D3), 6823–6836, doi:10.1029/95JD03523.
- Proffitt, M. H., and R. J. McLaughlin (1983), Fast-response dual-beam UV-absorption ozone photometer suitable for use on stratospheric balloons, *Rev. Sci. Instrum.*, *54*(12), 1719–1728, doi:10.1063/1.1137316.
- Ridley, B., et al. (2004a), Convective transport of reactive constituents to the tropical and mid-latitude tropopause region: I. Observations, *Atmos. Environ.*, *38*(9), 1259–1274, doi:10.1016/j.atmosenv.2003.11.038.
- Ridley, B., et al. (2004b), Florida thunderstorms: A faucet of reactive nitrogen to the upper troposphere, *J. Geophys. Res.*, *109*, D17305, doi:10.1029/2004JD004769.
- Schumann, U., and H. Huntrieser (2007), The global lightning-induced nitrogen oxides source, *Atmos. Chem. Phys.*, *7*(14), 3823–3907, doi:10.5194/acp-7-3823-2007.
- Seinfeld, J. H., and S. N. Pandis (2006), *Atmospheric Chemistry and Physics: From Air Pollution to Climate Change*, 2nd ed., 1203 pp., John Wiley, Hoboken, N. J.
- Skamarock, W. C., J. G. Powers, M. Barth, J. E. Dye, T. Matejka, D. Bartels, K. Baumann, J. Stith, D. D. Parrish, and G. Hubler (2000), Numerical simulations of the July 10 Stratospheric-Tropospheric Experiment: Radiation, Aerosols, and Ozone/Deep Convection Experiment convective system: Kinematics and transport, *J. Geophys. Res.*, *105*(D15), 19,973–19,990, doi:10.1029/2000JD900179.
- Stenchikov, G., R. Dickerson, K. Pickering, W. Ellis, B. Doddridge, S. Kondragunta, O. Poulida, J. Scala, and W.-K. Tao (1996), Stratosphere-troposphere exchange in a midlatitude mesoscale convective complex: 2. Numerical simulations, *J. Geophys. Res.*, *101*(D3), 6837–6851, doi:10.1029/95JD02468.
- Tao, W.-K., J. Simpson, and M. McCumber (1989), An ice-water saturation adjustment, *Mon. Weather Rev.*, *117*(1), 231–235, doi:10.1175/1520-0493(1989)117<0231:AIWSA>2.0.CO;2.
- Tewari, M., F. Chen, W. Wang, J. Dudhia, M. A. LeMone, K. Mitchell, M. Ek, G. Gayno, J. Wegiel, and R. H. Cuenca (2004), Implementation and verification of the unified NOAA land surface model in the WRF model, paper presented at the 20th Conference on Weather Analysis and Forecasting/16th Conference on Numerical Weather Prediction, Am. Meteorol. Soc., Seattle, Wash., 11–15 Jan.
- Zhang, R., X. Tie, and D. W. Bond (2003), Impacts of anthropogenic and natural NO_x sources over the U.S. on tropospheric chemistry, *Proc. Natl. Acad. Sci. U.S.A.*, *100*(4), 1505–1509, doi:10.1073/pnas.252763799.